Journal of Power Sources 182 (2008) 353–358

Contents lists available at ScienceDirect

Journal of Power Sources

journal homepage: www.elsevier.com/locate/jpowsour

Short communication

Electrochemical properties of melt-spun Al–Si–Mn alloy anodes for lithium-ion batteries

Z.B. Sun [a], X.D. Wang [a], X.P. Li [a], M.S. Zhao [b], Y. Li [b], Y.M. Zhu [a], X.P. Song [a,*]

[a] School of Science, State Key Laboratory for Mechanical Behavior of Materials, Xi'an Jiaotong University, Xi'an 710049, PR China
[b] School of Materials Science and Engineering, Henan University of Science and Technology, Luoyang 471003, PR China

ARTICLE INFO

Article history:
Received 5 January 2007
Received in revised form 17 March 2008
Accepted 23 March 2008
Available online 29 March 2008

Keywords:
Al–Si–Mn alloy
Melt spinning
Microstructure
Lithium-ion battery
Electrochemical property

ABSTRACT

$Al_{60-X}Si_{40}Mn_X$ (X = 0, 1, 3, 5, 7 and 10 at.%) ribbons were prepared by melt spinning. A supersaturated solid solution of Si and Mn in fcc α-Al with very fine microstructures have been obtained in the ribbons. The electrochemical measurements have revealed that the Al–Si–Mn alloys with some compositions can exhibit a high Li inserting specific capacity and stable cycle performance. A specific capacity of more than 500 mAh g^{-1} and the cycle efficiency of 90% have been achieved in melt-spun $Al_{55}Si_{40}Mn_5$ and $Al_{53}Si_{40}Mn_7$ alloys after 10 cycles. An ordered phase, δ′ (Al_3Li), seems to be formed in the alloys after Li inserting, whereas no other compounds with Li have been detected. It is evident that the supersaturated solid solution plays the main role in improving the specific capacity and cycle performance. Refinement of grains could facilitate the diffusion of Li atoms. The coexistence of multi-phases has limited the alloy volume expansion during Li inserting. As a result, a high-specific capacity and a stable cycle performance have been achieved.

1. Introduction

Lithium-ion batteries are the best commercial rechargeable batteries due to their high-specific capacity and excellent cycle performance. It is well known that the properties of the batteries strongly depend on anode materials. For an anode material of commercial lithium-ion batteries, graphite is the most popular choice. Its theoretical specific capacity is 372 mAh g^{-1} [1–3].

Some investigations have revealed that some metallic and submetallic crystals, such as Si and Sn, exhibit much higher specific capacities than graphite due to the formation of intermetallic compounds with Li. For example, $Li_{22}Si_5$ has a theoretical specific capacity of 4200 mAh g^{-1} [4,5], $Li_{22}Sn_5$, 994 mAh g^{-1} [6,7] and Li_3Sb, 900 mAh g^{-1} [8]. These crystals are then defined as active materials for Li inserting. However, it has been found that the cycle performance of pure Si, Sn, Sb, etc. are much inferior to graphite. It is currently considered that the larger volume expansion takes place during the formation of intermetallic compounds [4–8]. As a result, cracking or pulverization will occur to the metallic or submetallic anode materials during Li inserting or extracting, resulting in a poor cycle performance [9]. Therefore, a large amount of research has focused on the methods for improving the cycle performance of these materials. So far, many intermetallic compounds, such as Cu_6Sn_5 [10], Al_6Mn [11], Mg_2Si [12], Ag_3Sb [13] and $Ag_{36.4}Sb_{15.6}Sn_{48}$ [14], have been attempted. The cycle performance has been improved to some degree. In these studies, thin films exhibit excellent cycle performance and high-specific capacity. Dahn and collaborators have accomplished a lot of distinctive work in this field [9,15–19].

According to the Al–Li binary alloy diagram [20], the solubility of Li in fcc Al is about 1 at.% at 373 K. AlLi, Al_2Li_3 and Al_4Li_9 compounds can form, which depends on the alloy compositions. Suresh et al. [21] and Bang et al. [22] studied the electrochemical properties of pure Al and AlLi alloys, respectively. Although the cycle performance data were not published, Al was considered as an electrode material for Li batteries [22,23]. Hamon et al. [23] investigated the electrochemical properties of Al thin films, and found a high performance when the thickness was very thin. However, the properties would also become inferior with increasing thickness of the films. Lindsay et al. prepared Fe_2Al_5 powders in order to improve the cycle performance by adding the inactive element Fe [24]. The first discharge specific capacity was 485 mAh g^{-1}, but declined to about 140 mAh g^{-1} after two cycles. Fleischauer et al. [16,25] prepared Al–Si–Mn crystalline and amorphous films with different compositions. The thin films exhibited a high discharge specific capacity and an improved cycle performance. These investigations have indicated that Al-based alloys are promising anode materials for Li-ion battery if their cycle properties are improved.

* Corresponding author. Tel.: +86 29 82665892; fax: +86 29 83237910.
E-mail addresses: shadowspring@gmail.com, xpsong@mail.xjtu.edu.cn (X.P. Song).

0378-7753/$ – see front matter.
doi:10.1016/j.jpowsour.2008.03.053

In this work, $Al_{60-X}Si_{40}Mn_X$ (X = 0, 1, 3, 5, 7 and 10 at.%) alloys were prepared by melt spinning. The as-quenched alloys can exhibit a stable cycle performance with a high charge–discharge specific capacity.

2. Experimental

Pure aluminum (99.97%), pure silicon (99.99%) and pure manganese (99.93%) were used to prepare the Al–Si–Mn alloys. The mater alloys were prepared in an arc-melting furnace with a non-consumable tungsten electrode. In order to obtain homogeneous samples, several remelting cycles were performed with reversing the ingots before each remelting. Subsequently, the ingots with a mass of about 20 g were put into a quartz tube. After the ingots were inductively melted and heated to the required temperature, the alloy ribbons were then prepared by single roller melt spinning under a pressure of 0.5 atm Ar gas. The obtained ribbons were 3 mm wide and 20–30 μm thick.

The phase constitution and microstructures of the ribbons were analyzed by a Rigaku D/max 2400 X-ray diffractometer and a Hitachi H-800 transmission electron microscope (TEM). The foil specimens used for TEM were prepared by ion polishing.

The as-quenched ribbons were prepared into powders by ball milling under Ar gas atmosphere. Subsequently, carbon black was added into the powders and mixed homogenously. The admixture was dispersed in *N*-methylpyrrolidinone (NMP) added by polyvinylidene fluoride (PVDF). The mass ratio of the powders, carbon black and PVDF was 84:8:8. The slurry was spread on the copper foil to prepare electrodes. The electrodes were dried in a vacuum drying box at 398 K for 10 h to remove the solvent. An electrode and a counter electrode plate of pure lithium were assembled into a simulative battery in Ar gas. The employed electrolyte is a solution of 1 mol L^{-1} $LiPF_6$ in ethylene carbonate (EC) and dimethyl carbonate (DMC). The ratio of EC and DMC is 1:1 (w/w). The electrochemical properties of simulative battery were measured by a BT-2000 Arbin Instrument. The surface morphology of the electrode after Li inserting was observed by a JSM 6460 scanning electron microscope (SEM).

3. Results

Fig. 1a shows an X-ray diffraction (XRD) pattern of as-quenched $Al_{60}Si_{40}$ ribbons. The diffraction peaks of α-Al and α-Si appear. The

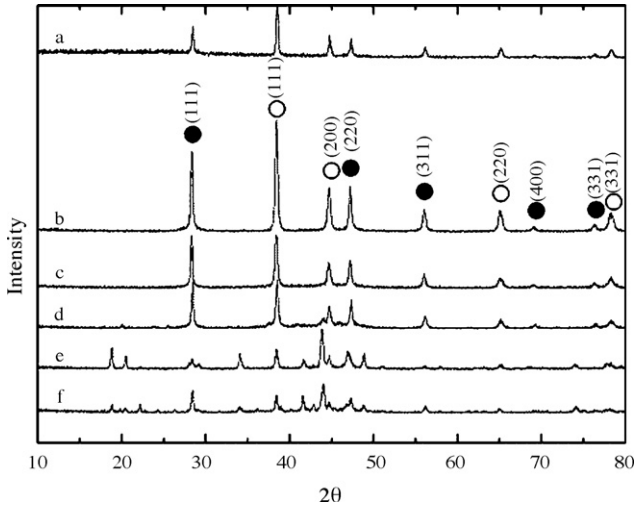

Fig. 1. X-ray diffraction patterns of as-quenched $Al_{60}Si_{40}$ (a), $Al_{59}Si_{40}Mn_1$ (b), $Al_{57}Si_{40}Mn_3$ (c), $Al_{55}Si_{40}Mn_5$ (d), $Al_{53}Si_{40}Mn_7$ (e) and $Al_{50}Si_{40}Mn_{10}$ (f) ribbons. (○) α-Al and (●) α-Si. The other peaks are from metastable Al–Si–Mn compound.

Table 1
Lattice parameter (a) of α-Al in melt-spun Al–Si–Mn ribbons

Composition (at.%)	a (nm)
$Al_{60}Si_{40}$	0.4042
$Al_{59}Si_{40}Mn_1$	0.4043
$Al_{57}Si_{40}Mn_3$	0.4044
$Al_{55}Si_{40}Mn_5$	0.4040
$Al_{53}Si_{40}Mn_7$	0.4041
$Al_{50}Si_{40}Mn_{10}$	0.4041

lattice parameter of α-Al in the ribbons is 0.4042 nm, less than that of pure Al (0.4049 nm). Except α-Al and α-Si, other diffraction peaks are not detected in as-quenched $Al_{59}Si_{40}Mn_1$ and $Al_{57}Si_{40}Mn_3$ ribbons, as shown in Fig. 1b and c. For $Al_{55}Si_{40}Mn_5$ ribbons, a weak diffraction peak close to $(2\,0\,0)_{Al}$ appears, seeing Fig. 1d. When Mn contents increase to 7 and 10%, many diffraction peaks different from those of α-Al and α-Si appear, as presented in Fig. 1e and f. The lattice parameters of α-Al in Al–Si–Mn ribbons are less than those pure Al, as listed in Table 1.

The microstructures of as-quenched $Al_{60}Si_{40}$ ribbons are illustrated in Fig. 2a. The matrix is α-Al with a mean diameter of about 1 μm. The particles distributing in the matrix, as marked by arrow A, is α-Si. After the as-quenched ribbons are annealed at 573 K for 3 h, a lot of finer Si particles can be observed, as denoted by arrow B in Fig. 2b. In combination with the XRD results, it can be determined that the α-Al in the $Al_{60}Si_{40}$ ribbons is supersaturated.

Fine α-Al grains with a mean diameter of less than 500 nm are observed in $Al_{59}Si_{40}Mn_1$ ribbons, as denoted by arrow A in Fig. 3a. The α-Al grains are further refined when Mn content increases to 3% ($Al_{57}Si_{40}Mn_3$), as can be seen in Fig. 3b. The intergranular zones are also identified as α-Al phase, where the bright and dark stripe contrast is caused by the segregation of Si and Mn, as marked by arrow B in Fig. 3a. The phase marked by arrow C is α-Si. For $Al_{57}Si_{40}Mn_3$ ribbons, an unidentified phase is formed between α-Al grains (arrow D in Fig. 2b). For $Al_{55}Si_{40}Mn_5$ ribbons, α-Al grains are refined to less than 50 nm, but coarse Si particles with a diameter of 1 μm can be still observed. Some fine black particles distribute between α-Al grains, seeing Fig. 4a. When Mn content is increased to 7%, TEM analysis indicates that a needle-shaped phase appears and the coarse Si particles disappear, as shown in Fig. 4b. α-Al grains, fine α-Si particles and some black particles of another phase distribute between the needles. The sizes of the three phases are all less than 100 nm. Selected area diffraction has not identified this needle-shaped phase. According to Refs. [26–28] and the XRD results, we can deduce that the needle-shaped phase in Fig. 4b, the black particles in Fig. 4a and the phase marked by arrow D in Fig. 2b are probably metastable Al–Si–Mn compounds formed during rapid solidification. The microstructures of $Al_{50}Si_{40}Mn_{10}$ ribbons are similar to those of $Al_{53}Si_{40}Mn_7$.

It is very clear that increasing Mn content can refine α-Al grains. Meanwhile, the volume fraction of α-Al decreases with increasing Mn due to the formation of more Al–Si–Mn compounds. For Al–Si–Mn alloys, several phase transformation steps will take place during cooling from the liquid zone to room temperature. But the phase transformations in these experiments have not been completed due to the rapid cooling and the equilibrium compounds are not formed.

Fig. 5 illustrates the specific capacities of melt-spun $Al_{60-X}Si_{40}Mn_X$ alloys depending on cycle numbers. The cells were tested under a constant current density of 0.1 mA cm^{-2}. In the first cycle, the lowest discharge voltage was 0.13 V. Through this process, the electrode materials could be activated. Subsequently, the lowest discharge voltage of 0.03 V was set in further cycles.

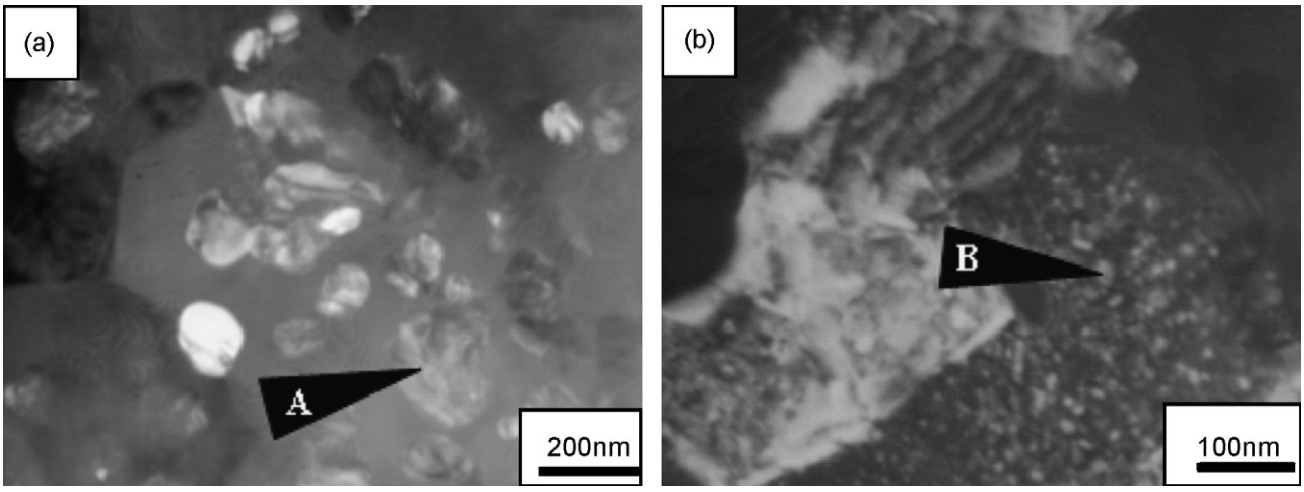

Fig. 2. Microstructures of melt-spun $Al_{60}Si_{40}$ ribbons (dark field). The arrow A denotes α-Si solidified from melt and B denotes Si precipitates.

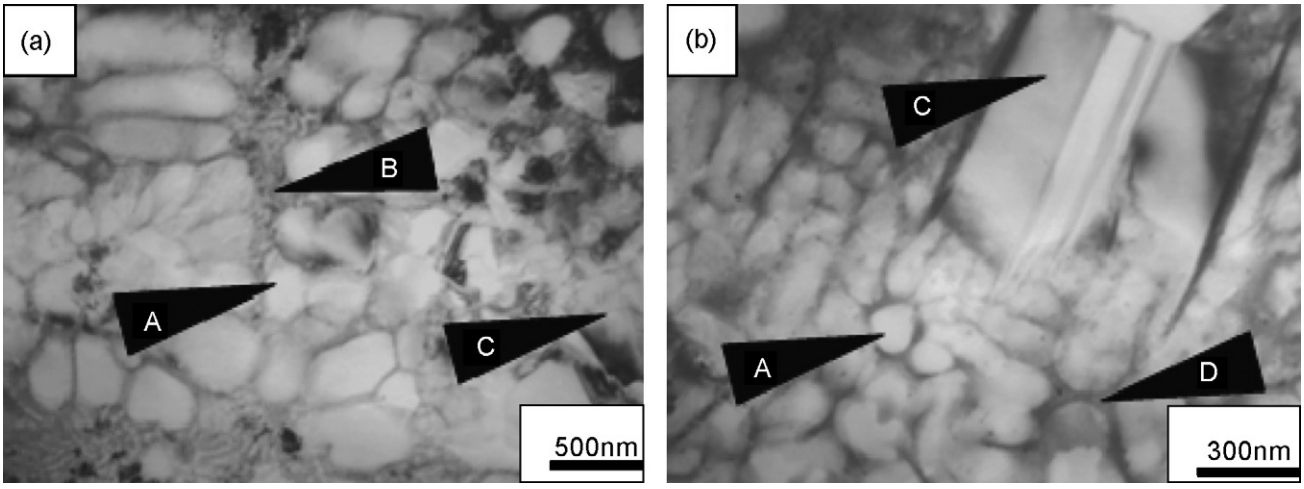

Fig. 3. Microstructures of melt-spun $Al_{59}Si_{40}Mn_1$ (a) and $Al_{57}Si_{40}Mn_3$ ribbons (b). Arrows A and B denote α-Al, C denotes α-Si and D denotes Al–Mn–Si compound.

For melt-spun $Al_{60}Si_{40}$ alloy, the specific capacity of the first discharge can reach 1660 mAh g^{-1} and declines rapidly to 40 mAh g^{-1} after 10 cycles, as shown in Fig. 5. The specific capacity of the first discharge is 1803 mAh g^{-1} and declines to125 mAh g^{-1} after 10 cycles for $Al_{59}Si_{40}Mn_1$ alloy. When the Mn content is increased to 3% ($Al_{57}Si_{40}Mn_3$), a specific capacity of 200 mAh g^{-1} could be kept after 10 cycles. For $Al_{55}Si_{40}Mn_5$ alloy, the specific capacity of the first discharge is 1089 mAh g^{-1}. However, a specific capacity

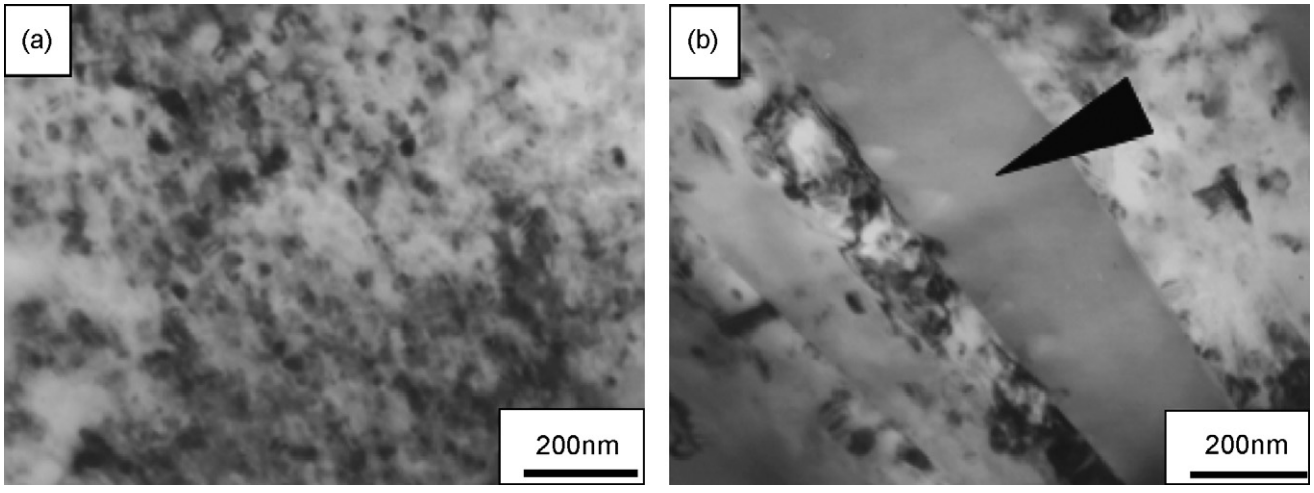

Fig. 4. Microstructures of melt-spun $Al_{55}Si_{40}Mn_5$ (a) and $Al_{53}Si_{40}Mn_7$ ribbons (b). The arrow denotes an Al–Si–Mn compound.

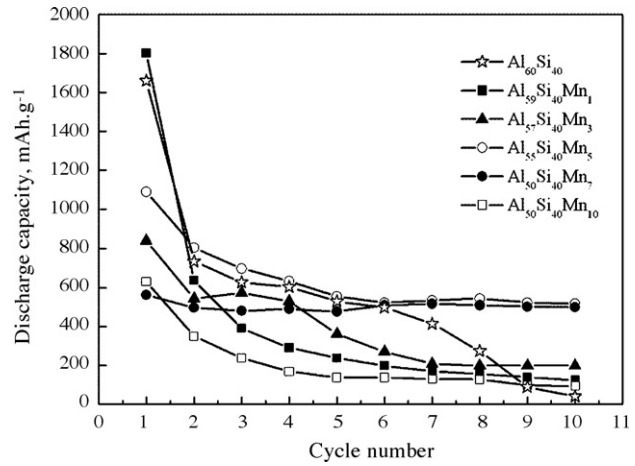

Fig. 5. Discharge specific capacity of melt-spun Al–Si–Mn alloys depending on cycle number.

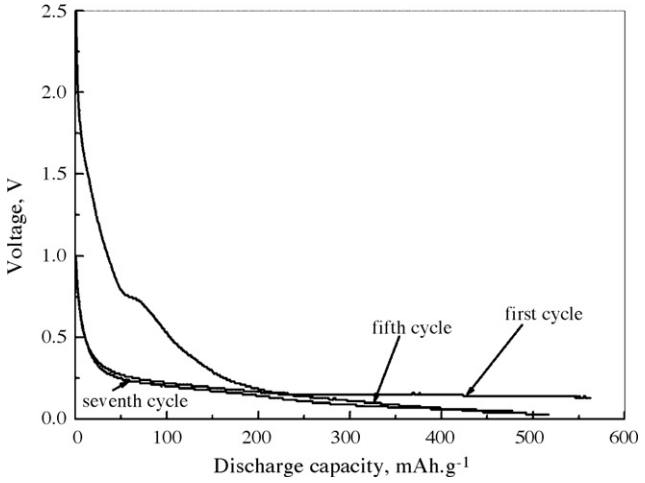

Fig. 6. Voltage curves of melt-spun $Al_{55}Si_{40}Mn_7$ alloy depending on the discharge specific capacity.

becomes 518 mAh g^{-1} after 10 cycles. When Mn content increased to 7%, a very stable specific capacity curve and a specific capacity of 500 mAh g^{-1} have been obtained after 10 cycles. However, the specific capacity declines when the Mn content is further increased to 10%, although the cycle performance is stable.

The voltage versus discharge specific capacity curves of melt-spun $Al_{55}Si_{40}Mn_7$ alloy anodes are shown in Fig. 6. The discharge profiles of met-spun Al–Si–Mn alloys for the 1st, 5th and 7th cycles are similar to that of pure Al reported by Hamon et al. [23], except that the discharge voltage plateau of Al–Si–Mn alloys is slightly lower.

After Li atoms insert into melt-spun Al–Si alloy, a very interesting result has been achieved. The diffraction peaks of α-Al and α-Si are obtained and no Li–Si or Li–Al intermetallic compounds are detected, as shown in Fig. 7. However, a weak peak appears, as designated by '▽' in Fig. 7. This diffraction peak seems to accord with one of the ordered δ′ (Al_3Li) phase reported in the work [29] and [30]. δ′ forms in the spinodal separation of Al–Li alloys. The melt-spun $Al_{55}Si_{40}Mn_5$ alloy has a similar diffraction peak, as illustrated in Fig. 8b. After Li extracting, this peak becomes weaker, seeing Fig. 8c. Table 2 lists the lattice parameters of α-Al in $Al_{60}Si_{40}$ and $Al_{55}Si_{40}Mn_5$ after Li inserts and extracts. The lattice parameter of α-Al in the as-quenched ribbons is re-listed for comparison. The insertion of Li atoms has increased the lattice parameter of

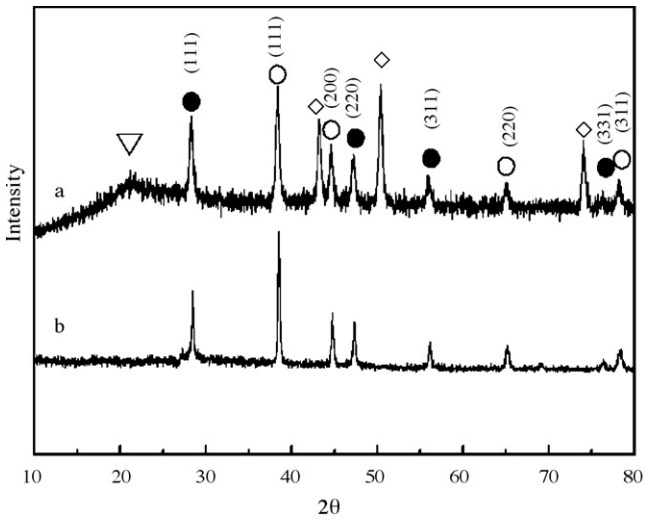

Fig. 7. X-ray diffraction patterns of as-quenched $Al_{60}Si_{40}$ ribbons (a) and the anodes inserted by Li (b). (◯) α-Al, (●) α-Si, (▽) δ′ and (◊) copper foil.

α-Al. This result indicates that a solid solution of Li in α-Al has formed.

The SEM analysis indicates that some cracks form in the melt-spun Al–Si–Mn anodes before Li inserting, as shown in Fig. 9a. After the alloys experience 10 cycles, the cracks in $Al_{60}Si_{40}$ and $Al_{59}Si_{40}Mn_1$ alloys become more, as shown in Fig. 9b. In the case of $Al_{55}Si_{40}Mn_5$ and $Al_{53}Si_{40}Mn_7$ alloys, the cracks have a smaller increase, seeing Fig. 9c.

An evident improvement of cycle performance has been achieved in the melt-spun Al–Si–Mn alloys in comparison with pure Si or Fe_2Al_5 powders. According to the classical diffusion theories [31], a new phase forms on the surface layer during Li inserting into

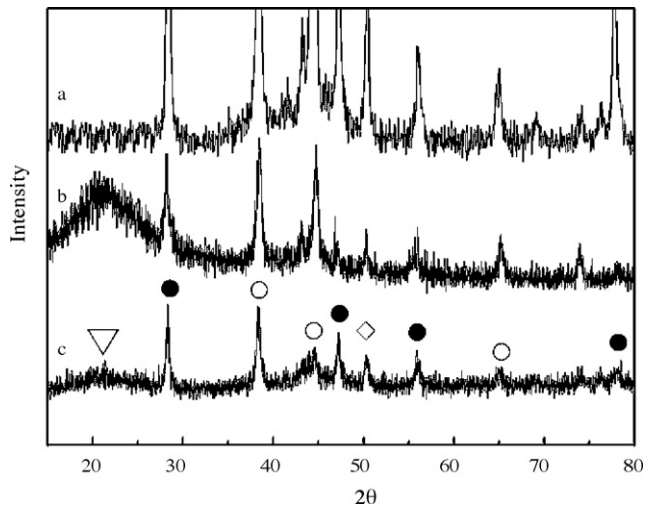

Fig. 8. X-ray diffraction patterns of melt-spun $Al_{55}Si_{40}Mn_5$ alloy: (a) pristine, (b) Li inserting and (c) Li extracting. (◯) α-Al, (●) α-Si, (▽) δ′ and (◊) copper foil.

Table 2
Lattice parameter (nm) of α-Al after Li inserting and extracting for 10 times

	Samples	
	$Al_{60}Si_{40}$	$Al_{55}Si_{40}Mn_5$
As-quenched ribbon	0.4042	0.4040
Li insertion	0.4049	0.4053
Li extraction	–	0.4045

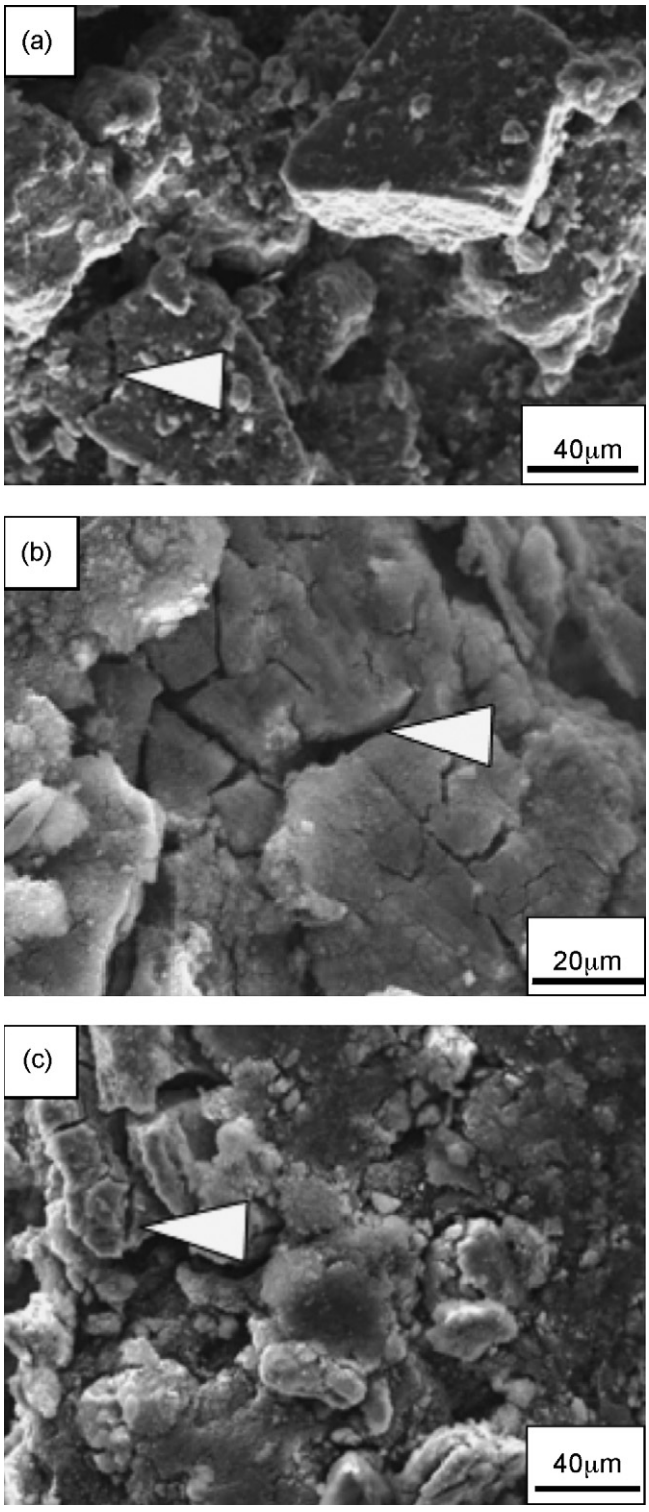

Fig. 9. SEM images of melt-spun Al–Si–Mn alloy anodes: (a) $Al_{60}Si_{40}$ before Li inserting, (b) $Al_{60}Si_{40}$ after 10 cycles and (c) $Al_{55}Si_{40}Mn_5$ after 10 cycles. The arrow denotes the cracks.

some pure metals, such as Al, Si, Sn, Zn, and so on. This process is a typical reaction diffusion. A volume expansion will be inevitable. In this study, an supersaturated Al-based solid solution with two or three components has been obtained. According to classical thermodynamics [31], two or three phases could co-exist in the solid solution during reaction diffusion. A solid solution of Li in the α-Al will firstly form as Li inserts into the melt-spun Al–Si–Mn solid solution anodes. When the Li content in Al solid solution exceeds the solubility limit, it is likely that the δ′ phase forms and co-exists with Al(Li) solid solution. On the basis of the Al–Li binary phase diagram, the solubility of Li in α-Al is about 1% at 373 K. But the solubility can be increased to about 5.5% due to the coexistence of α-Al and δ′ [30]. As a result, a larger concentration gradient can be established, facilitating the diffusion of Li atoms into deeper layer of α-Al gains. However, when α-Al grains are coarser, take $Al_{60}Si_{40}$ and $Al_{59}Si_{40}Mn_1$ alloys for example, the transport of Li relies on the volume diffusion. Because the volume diffusion velocity of atoms in a solid is very slow at room temperature, the electrodes overcharge easier. The expansion still focuses on the surface layer and causes local cracks and the specific capacity will attenuate rapidly (Fig. 5). When α-Al grains are refined to nano-size, the transport of Li mainly depends on the interface diffusion. As a result, the diffusion of Li atoms is further facilitated into the deeper layer of alloy powders. The Al–Si–Mn compounds between the α-Al grains in nano-size will also limit the volume expansion. The cycle performance is then improved. For $Al_{53}Si_{40}Mn_7$ alloy, the needle-shaped Al–Si–Mn compound acts as a framework, which can decrease the volume expansion. And hence, the cycle performance is very stable (Fig. 5).

No evidence indicates that the metastable Al–Si–Mn compounds formed in the ribbons are Li storage phases. This result is consistent with the study of Fleischauer et al. [28]. No Li–Si compounds form after Li atoms inserting into the anodes prepared from the melt-spun Al–Si–Mn alloys. Supposing all the Al atoms have formed δ′(Al_3Li), specifically for $Al_{55}Si_{40}Mn_5$, the calculated specific capacity is only 167 mAh g^{-1}, less than the measured value in present work. It can be deduced that many Li atoms have storied at the interfaces. This will not result in a damage of lattice, and therefore, the cycle performance of the melt-spun Al–Si–Mn anode materials can be further improved. It is easy to understand the low-specific capacity of melt-spun $Al_{50}Si_{40}Mn_{10}$ alloy. The volume fraction of the active phases (α-Al) decreases too much due to the formation of more metastable Al–Si–Mn compounds in this alloy.

4. Conclusions

Stable cycle performance has been achieved in melt-spun Al–Si–Mn alloys. The formation of supersaturated solid solution of Si and Mn in α-Al has prevented the crystal lattice from being destroyed. Refining α-Al grains can facilitate diffusion of Li atoms and improve the Li storage ability. The formation of metastable Al–Si–Mn compounds plays an important role in limiting volume expansion.

Acknowledgement

Supported by the National Natural Science Foundation of China (50371066).

References

[1] C. Menachem, E. Peled, L. Burstein, Y. Rosenberg, J. Power Sources 277–282 (1997) 68.
[2] T.D. Hatchard, M.N. Obrovac, J.R. Dahn, J. Electrochem. Soc. 152 (2005) A2335.
[3] A. Bonakdarpour, K.C. Hewitt, R.L. Turner, J.R. Dahn, J. Electrochem. Soc. 151 (2004) A470.
[4] H. Dong, X.P. Ai, H.X. Yang, Electrochem. Commun. 5 (2003) 952.
[5] Y.H. Lee, S.M. Lee, Electrochem. Commun. 6 (2004) 465.
[6] N. Tamura, R. Ohshita, M. Fujimoto, S. Fujitani, M. Kamino, I. Yonezu, J. Power Sources 107 (2002) 48.
[7] Y. Wang, J.Y. Lee, T. Deivarai, J. Electrochem. Soc. 151 (2004) A1804.
[8] L. Aldon, A. Garcia, J. Olivier-Fourcade, J. Jumas, F.J. Fernández-Madrigal, P. Lavela, C.P. Vicente, J.L. Tirado, J. Power Sources 119–121 (2003) 585.
[9] M. Winter, J.O. Besenhard, Electrochim. Acta 45 (1999) 31–50.

[10] K.D. Kepler, J.T. Vaughey, M.M. Thackeray, Electrochem. Solid-State Lett. 2 (1999) 307.
[11] D. Shechtman, I. Blech, D. Gratias, J.W. Cahn, Phys. Rev. Lett. 53 (1984) 1951.
[12] J.T. Vaughey, L. Fransson, H.A. Swinger, K. Edström, M.M. Thavkeray, J. Power Sources 119–121 (2003) 64.
[13] E. Ronnebro, J.T. Yin, A. kitano, M. Wada, S. Tanase, T. Sakai, Electrochem. Soc. 152 (2005) A152–A157.
[14] J. Yin, M. Wada, S. Tanase, T. Sakai, Electrochem. Soc. 151 (2004) A867.
[15] Z.H. Chen, V. Chevrier, L. Christensen, J.R. Dahn, Electrochem. Solid-State Lett. 7 (2004) A310.
[16] M.D. Fleischauer, J.R. Dahn, J. Electrochem. Soc. 151 (2004) A1216.
[17] M.D. Fleischauer, J.M. Topple, J.R. Dahn, Electrochem. Solid-State Lett. 8 (2005) A137.
[18] M.D. Fleischauer, M.N. Obrovac, J.D. Mcgraw, R.A. Dunlap, J.M. Topple, J.R. Dahn, J. Electrochem. Soc. 153 (2006) A484.
[19] T.D. Fatchard, J.M. Topple, M.D. Fleischauer, J.R. Dahn, Electrochem. Solid-State Lett. 6 (2003) A129.
[20] H. Okamoto, Phase Diagrams Binary Alloys (2000) 35.
[21] P. Suresh, A.K. Shukla, S.A. Shivashankar, N. Munichanhraiah, J. Power Sources 110 (2002) 11.
[22] H.J. Bang, S. Kim, J. Prakash, J. Power Sources 92 (2001) 45.
[23] Y. Hamon, T. Brousse, F. Joousse, P. Topart, P. Buvat, D.M. Schleich, J. Power Sources 97/98 (2001) 185.
[24] M.J. Lindsay, G.X. Wang, H.K. Liu, J. Power sources 119–121 (2003) 84.
[25] M.D. Fleischauer, M.N. Obrovac, J.R. Dahn, J. Electrochem. Soc. 153 (2006) A1201.
[26] R. Hambeleton, H. Jones, W.M. Rainforth, Mater. Sci. Eng. A A226–228 (1997) 157.
[27] N. Krendelsberger, F. Weitzer, J. Schuster, Metall. Mater. Trans. A 33A (2002) 3311.
[28] D.M.J. Wilkes, H. Jones, J. Mater. Sci. 34 (1999) 735.
[29] V. Radmilovic, A.G. Fox, G. Thomas, Acta Metall. 37 (1989) 2385.
[30] B. Noble, S.E. Bray, Acta Metall. 46 (1998) 6163.
[31] P. Haasen, Physical Metallurgy, University Press, Cambridge, 1986, 187.